Compressive behaviour of double skin sections with stainless steel outer tubes and recycled aggregate concrete

D.S. Castanheira [a,b], L.R.O. de Lima [c], P.C.G. da S. Vellasco [c], K.A. Cashell [d,*], L. Gardner [b]

[a] PGECIV – Civil Engineering Post-Graduate Program, UERJ – State University of Rio de Janeiro, Brazil
[b] Department of Civil and Environmental Engineering Imperial College London, London, UK
[c] Structural Engineering Department, UERJ – State University of Rio de Janeiro, Brazil
[d] Department of Civil and Environmental Engineering Brunel University London, London, UK

ARTICLE INFO

ABSTRACT

An experimental and numerical study into the behaviour of concrete-filled double skin tubular (CFDST) stub columns is presented. A total of eight axial compression tests were carried out, four utilising conventional concrete and four with recycled aggregate concrete. The stub columns were circular in cross-section and each comprised an austenitic stainless steel outer tube and a carbon steel inner tube, of varying dimensions. Accordingly, hollow ratios of 0.67 and 0.55 were considered. The recycled coarse aggregate was made by crushing test specimens from a previous research project, and a replacement ratio of 50% was adopted. During the experiments, similar structural behaviour and failure modes were observed between the specimens with conventional and recycled aggregate concrete. To investigate the behaviour further, a finite element model was developed in ABAQUS; validation of the model against the experimental results from the current work as well as data available in the literature is described. The finite element model was employed to conduct a parametric study to examine the load-bearing contributions of the constituent components of CFDST sections and to assess the influence of the hollow ratio on the structural behaviour. The experimental and numerical ultimate loads are compared with the capacity predictions determined using available design procedures. Overall, the results show that CFDST stub columns with recycled aggregate concrete can achieve similar capacities to their conventional concrete counterparts, demonstrating the potential for the wider use of recycled aggregate concrete, towards more sustainable structural solutions.

1. Introduction

Concrete-filled double skin tubular (CFDST) sections comprise two steel tubes with different dimensions concentrically positioned, one inside the other, and concrete infill in the space between the sections. This type of composite member can be formed from different tubular shapes, including square, rectangular, circular or elliptical sections. CFDST members are suitable for use in a range of structural applications, such as offshore platforms, bridge piers, high-rise buildings and transmission towers, and have been the focus of significant research interest in recent years [e.g. 1–4]. Their advantages are similar to those of concrete-filled steel tubular (CFST) columns, and include high compressive load-carrying capacity and good ductility, benefitting from the confining effect of the steel tubes on the concrete infill and the delay to local buckling of the steel tubes owing to the restraining effect of the concrete

[3,5], as well as excellent fire resistance [4]. In addition, CFDST columns can be lighter and more efficient, with lower construction costs, compared with other structural solutions like CFST columns owing to the reduced material usage [3].

The current paper is concerned with the behaviour of CFDST columns with circular stainless steel outer tubes, circular carbon steel inner tubes and recycled aggregate concrete (RAC) for the infill. Stainless steel is a popular material for structural engineering applications owing to its many favourable attributes compared with carbon steel, including excellent corrosion resistance, high strength and ductility, improved fire resistance, low maintenance requirements and aesthetic appeal [6,7]. Stainless steel is also fully recyclable and has an excellent rate of recycling because of its high residual value.

The use of concrete with recycled aggregates is currently receiving significant attention from the research community. RAC is made from

---

demolition waste which would otherwise be condemned to landfill, thus reducing the requirements for new aggregate materials to be sourced. There are three main types of material used for recycled aggregates: crushed concrete, crushed masonry and mixed demolition debris [8]. Recycled aggregates should ideally be derived from crushed concrete when employed for structural elements, without any impurities in the composition such as gypsum and ceramics, to maintain good mechanical performance [9]. Similar to natural aggregates, the mechanical properties of recycled aggregates are important to the overall performance of RAC structural members. Moreover, the presence of any residual cement paste adhered to the recycled aggregate, the quality of the original material used in the demolished structure as well as the size and shape of the aggregates following the crushing process can affect the water absorption, density and porosity of the resulting concrete, which consequently affects the mechanical properties [9,10]. RAC is not only influenced by the mechanical properties of the recycled aggregates but also by the concrete mix and the percentage of recycled aggregates used in the mix, known as the replacement ratio. It has been shown that recycled aggregate concrete typically has a lower Young's modulus, compressive strength and tensile strength compared with conventional concrete [10,11].

The design of CFDST members is not currently covered by international design standards though a number of studies into their compressive behaviour have been carried out, e.g. [12–14]. Uenaka et al. [15] experimentally investigated the behaviour of CFDST columns with carbon steel for both the outer and the inner tubes and proposed an equation for the determination of their ultimate axial capacity. Han et al. [12] conducted more than 80 tests on CFDST columns, including members with stainless steel outer tubes and carbon steel inner tubes. Various parameters were studied in this programme, including different cross-sections and hollow ratios χ, where χ is determined as:

$$\chi = d/(D - 2t_{so}) \tag{1}$$

in which d and D are the diameters of the inner and outer tubes, respectively, and t_{so} is the thickness of the outer tube. It was shown [12] that, in general, the ultimate axial capacity increases with a reduction in χ whereas the ductility decreases. An equation for calculating the load-carrying capacity of double skin columns with stainless steel outer tubes, considering the hollow ratio, was proposed and is further examined in the current paper. The structural performance of circular CFDST columns with stainless steel outer tubes and high strength steel inner tubes has also been examined through physical testing and numerical modelling [13]. A range of different cross-section geometries and concrete grades was considered. It was found that current design provisions for CFST columns provide, with minor modification, reasonable capacity predictions for CFDST columns.

There have been a number of studies into the use of recycled aggregate concrete in composite elements in recent years, including CFST columns where there is a significant contribution made by the confined concrete to the overall performance [e.g. 11,16]. It has been shown that as the replacement ratio increases, the ultimate load and stiffness of composite columns generally decrease [16]. To date, there have been no studies into CFDST sections featuring a combination of stainless steel, carbon steel and recycled aggregate concrete. This is therefore the subject of the present paper. First, a series of experiments is described on CFDST stub columns with stainless steel outer tubes, carbon steel inner tubes and either conventional [17] or recycled aggregate concrete infill. Next, a numerical model is developed using the ABAQUS finite element (FE) analysis software [18]; the FE model is validated against the experimental results generated herein and further results from the literature. The validated model is then employed to conduct a

Table 1
Average measured dimensions and key results for the stub column test specimens.

Specimen	L (mm)	D (mm)	t_{so} (mm)	d (mm)	t_{si} (mm)	$N_{u,test}$ (kN)	$\delta_{u,test}$ (mm)
NAC1	550.0	168.3	2.8	88.9	5.5	1941	15.7
NAC2						1865	20.1
NAC3				108.4	4.5	1649	16.2
NAC4						1612	14.6
RAC1	500.0			88.9	5.5	2087	20.7
RAC2						2075	20.8
RAC3				108.4	4.5	1685	11.6
RAC4						1693	11.8

parametric study. Finally, the accuracy of current design expressions is examined based on the results from the experimental and numerical investigation.

2. Experimental programme

2.1. General

An experimental programme on circular CFDST stub columns with stainless steel outer tubes and carbon steel inner tubes was conducted in the Civil Engineering Laboratory at the State University of Rio de Janeiro (UERJ). A total of 8 stub column experiments, together with supporting material tests, were performed. The main objectives of the testing programme were to determine the cross-section ultimate resistances and to assess the influence of using RAC in place of conventional concrete for the infill. The outer tubes of all test specimens were cold-formed from grade 1.4307 austenitic stainless steel while the inner tubes were hot-rolled from grade VMB300 hot-rolled carbon steel. The dimensions of the tubes are given in Table 1, including the diameters of the outer D and inner d tubular sections, their respective thicknesses, t_{so} and t_{si}, as well as the overall lengths L. Four of the test specimens (NAC1-NAC4) contained natural aggregate concrete (NAC) [17] while the remaining four (RAC1-RAC4) were infilled with recycled aggregate concrete (RAC). By varying the diameter of the inner tube, two hollow ratios χ equal to 0.55 and 0.67 were considered. The expression for χ, as given in Eq. (1), was introduced by Han *et al.* [12] and it was advised that the ideal range for the hollow ratio of CFDST circular stub columns is between 0.5 and 0.7. The lengths of the tested stub columns were approximately three times the diameter of the outer tube, in accordance with Han *et al.* [12], to avoid any significant influence of global buckling. A view of the cross-sections is shown in Fig. 1. Small steel strips with a diameter of 5.5 mm were welded between the inner and outer tubes, as shown in Fig. 2, to maintain concentricity during concrete casting, as recommended by Wang *et al.* [13].

2.2. Concrete

The test specimens were cast in two series using the same basic concrete mix design, which is presented in Table 2. The first series contained natural coarse aggregate (NA) [17] whereas the second series had 50% of the NA replaced with the same amount of recycled coarse aggregate (RA). A superplasticiser was included in both mixes to make the concrete more workable, and the quantity was selected as 0.15% of the cement weight. The NAC and RAC reached average compressive cylinder strengths f_c of 30 and 33 MPa, respectively. These were determined by conducting compressive tests on at least eight cylindrical samples from each batch of concrete, on the same day that the corresponding stub columns were tested. This was 40 days after casting for

Fig. 1. CFDST test specimens before casting.

Table 2
Details of concrete mix design.

Mix proportions (relative to weight of cement)	NAC	RAC
Cement	1.00	1.00
Sand	2.29	2.29
NA	1.58	0.79
RA	0	0.79
Water (i.e. *w/c* ratio)	0.43	0.46
Superplasticizer	0.0015	0.0015

2.3. Tubular sections

The mechanical properties of the carbon steel inner tubes were measured by the manufacturing company. The steel was found to have a Young's modulus E of 200 kN/mm^2, yield strength f_y of 375 N/mm^2, ultimate strength f_u of 474 N/mm^2 and ultimate strain ε_u of 34%. The mechanical properties of the austenitic stainless steel outer tubes were obtained through tensile coupon testing at the State University of Rio de Janeiro (UERJ). A total of four repeat tests were conducted in accordance with EN 10002-1 [25] and the testing procedure for curved coupons recommended by Huang and Young [26], and the average values were determined for each property. The stainless steel was found to have a Young's modulus E of 197 kN/mm^2, yield strength f_y of 419 N/mm^2, ultimate strength f_u of 674 N/mm^2, ultimate strain ε_u of 39% and fracture strain, measured over a gauge length of 50 mm, ε_f of 59%. A typical stress–strain curve from the tensile tests on the stainless steel outer tube is depicted in Fig. 4. The average values of the strain hardening exponents, n and m, for use in the two-stage Ramberg-Osgood stress–strain model [27,28], were 6.5 and 2.0, respectively.

2.4. Initial geometric imperfections

Initial geometric imperfections are typically introduced into metallic sections during the manufacturing process and can reduce the capacity of members. In the current test programme, the geometric imperfections in the stainless steel tubes were measured using a displacement transducer, in accordance with the procedure outlined by Luquin [29]. The circular cross-sections were divided into four quadrants as shown in Fig. 5(a), and seven points along the lengths of the columns in each quadrant were measured as indicated in Fig. 5(b); the results are presented in Fig. 6 for (a) the 88.9 × 5.5 mm tube as employed in RAC1 and (b) the 108.4 × 4.5 mm tube used in RAC3. In all cases, the measured imperfections were <10% of the thickness of the tube.

2.5. Test setup and procedure

The tests were conducted using a 3000 kN displacement-controlled universal testing machine. The columns were placed concentrically in

the NAC columns and 30 days after casting for the RAC specimens. The higher strength of the RAC compared with the NAC is attributed to the recycled coarse aggregates having greater water absorption properties compared with the natural coarse aggregates, thus reducing the effective water/cement ratio and increasing the strength of the concrete. Variability in the water absorption properties of recycled aggregates has been recognised as a challenge in utilising these materials [19]. It is also possible that the quality of the original material also positively affected the compressive strength of the RAC [20]. In accordance with recommendations given in [20], the recycled aggregates were treated before casting by first sieving to ensure that the particles were the same size as the natural coarse aggregates and then adding water immediately prior to casting and mixing in the saturated condition.

The recycled aggregate was manufactured through the crushing of concrete elements from a previous experimental campaign [21], as shown in Fig. 3; the original concrete had an average compressive cylinder strength at 28 days of 41 MPa [21]. The characteristic properties of the aggregates used in the concrete were determined prior to casting in accordance with the relevant Brazilian standards [22–24], and the data are given in Table 3.
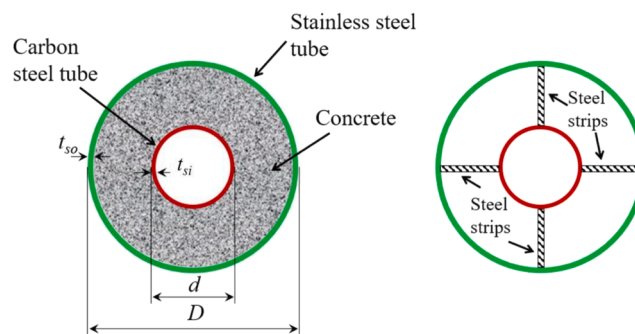

Fig. 2. Schematic view of CFDST cross-sections.

Fig. 3. Crushed concrete used as aggregate in the RAC.

Table 3
Characteristics of the coarse aggregates.

| Property	NAC	RAC
Fineness modulus (%)	5.6	5.6
Minimum diameter (mm)	4.8	4.8
Maximum diameter (mm)	9.5	9.5
Bulk density (kg/m^3)	1370	1090
Pore volume (%)	49.6	59.6
Specific gravity (kg/m^3)	2710	2700
Water absorption (%)	1.4	11.9
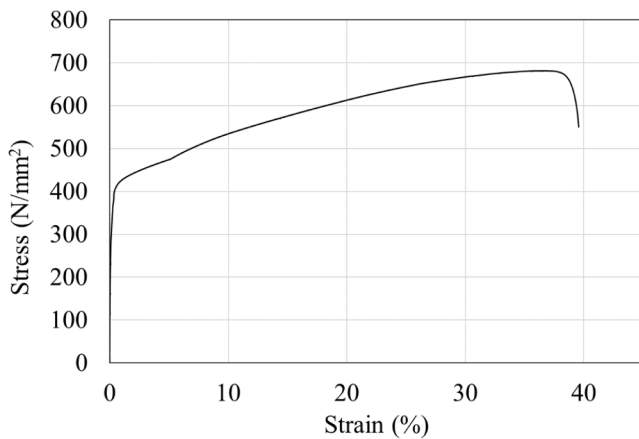
Fig. 4. Typical stress–strain response for austenitic stainless steel obtained from a tensile test on a coupon extracted from the outer tubular section.


(a)
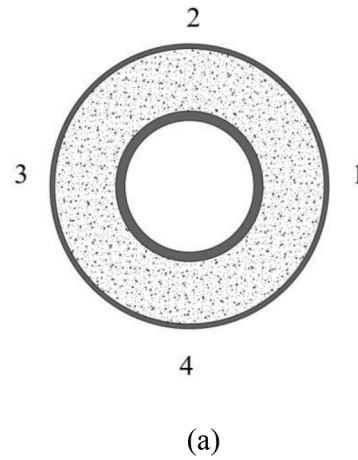
(b)

Fig. 5. Geometric imperfection measurement setup including (a) the four radial locations and (b) the seven longitudinal locations at which the measurements were taken.

the machine and an axial displacement was applied at a rate of 0.003 mm/s. Two plates, each with a thickness of 32 mm, were placed at either end of the columns. The bottom end of the columns had fixed boundary conditions. The top end had a ball seating that locked upon the application of load, hence also providing fixed boundary conditions. To avoid local failure at the member ends, circular ring stiffeners made from high strength steel were employed, similar to [30,31], as shown in Fig. 7. The instrumentation employed in the tests included four displacement transducers (LVDTs) and four strain gauges at the mid-height of the stub columns to obtain the transverse displacements and strains, respectively; two further LVDTs, positioned at the bottom plate, were
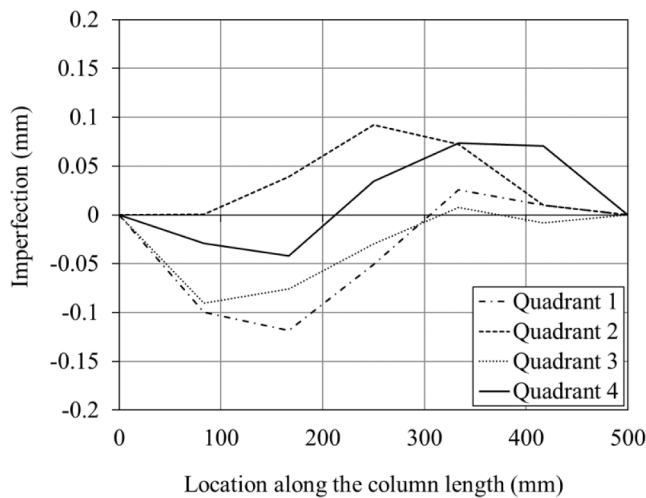
(a)
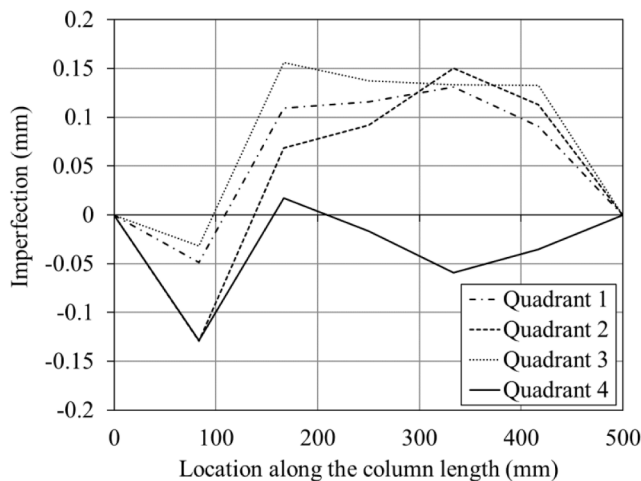
(b)

Fig. 6. Measured geometric imperfections along the stainless steel tubular column length for (a) the 88.9 × 5.5 mm tube as used for RAC1 and (b) the 108.4 × 4.5 mm tube as employed in RAC3.

employed to measure the longitudinal displacement, as shown in the schematic diagram in Fig. 7.

2.6. Results

The compressive behaviour of the CFDST stub columns was observed during the tests and the maximum loads ($N_{u,test}$) are presented in Table 1, as well as the corresponding axial displacement at $N_{u,test}$, $\delta_{u,test}$. It is clear that the columns with the smaller inner tubes and therefore larger volumes of concrete infill (i.e. NAC1, NAC2, RAC1 and RAC2) had greater ultimate load-carrying capacities compared with the columns with larger inner tubes and smaller concrete volumes (i.e. NAC3, NAC4, RAC3 and RAC4), as expected. In terms of the aggregate type, the stub columns with RAC generally achieved higher loads than the equivalent members with NAC, reflecting the higher strength of the RAC. Fig. 8 presents images of the CFDST stub columns after testing, showing the outward-only local buckling of the outer tubes, typically near the mid-height of the columns, accompanied by the suggestion of shear failure in the concrete. In Fig. 9, inward-only local buckling of the inner tube for specimen RAC1 was observed, showing that the presence of the infill

concrete restricted local buckling in one direction for both of the steel tubes. A similar failure mode was observed in all eight specimens.

2.6.1. Axial load versus axial displacement

Fig. 10 presents the experimental axial load *versus* axial displacement curves from all eight CFDST stub column tests. The axial displacement values were measured using two LVDTs on the bottom plate, as previously discussed, and the average values are presented. The results from specimens NAC1, NAC2, RAC1 and RAC2 (i.e. those with the smaller inner steel tubes) are shown in Fig. 10(a) while those from specimens NAC3, NAC4, RAC3 and RAC4 (i.e. those with the larger inner steel tubes) are shown in Fig. 10(b); the ultimate loads $N_{u,test}$ and corresponding displacements $\delta_{u,test}$ from all tests are presented in Table 1. The key observations from the figures are summarised as follows:

- Irrespective of the concrete type, all the specimens behaved in a similar manner, with comparable load–displacement responses and good ductility.
- The RAC specimens exhibited slightly stiffer responses and attained higher loads than their NAC counterparts.
- The CFDST specimens with the larger volumes of concrete (i.e. those presented in Fig. 10(a)) had greater load-carrying capacities, as expected, as well as more ductility, compared to those with the smaller concrete volumes.

2.6.2. Axial load versus average axial strain

Fig. 11 presents the experimental axial load *versus* average axial strain curves for (a) the specimens with the smaller inner tubes and therefore greater concrete volume and (b) those with the larger inner tubes. The average axial strains were determined as the mean measured value from the four strain gauges attached on the outer surface at the mid-height of each stub column. Strains were measured up to approximately 2% strain.

3. Numerical modelling

3.1. General

A numerical model was developed using the general-purpose finite element (FE) analysis package ABAQUS [18] to further investigate the behaviour of the studied CFDST cross-sections in compression. The development of the model is described in the subsections below, followed by a validation study using the test results from the experimental programme as well as relevant data from the literature. A parametric analysis is subsequently performed to investigate the influence of the key variables on the structural response of CFDST stub columns.

3.2. Model details

The CFDST stub columns were simulated using S4R shell elements [18] for the tubes and the circular steel rings and C3D8R solid elements [18] for the concrete infill. Following a mesh sensitivity study, uniform mesh sizes of 8 × 8 mm and 10 × 10 mm were employed for the tubes and the concrete infill, respectively. In order to simulate the fixed end conditions employed in the tests, the top surface of the modelled stub columns was coupled to a reference point through a rigid body constraint, where all degrees of freedom were restrained except for longitudinal translation. The compressive load was applied through a reference point at the bottom end of the stub columns. The Riks solution method was employed in the model to conduct a second order inelastic analysis (i.e. geometrically and materially nonlinear) with imperfections (GMNIA).

Initial geometric imperfections were included in the numerical analysis in the form of the lowest elastic eigenmode obtained from a prior linear buckling analysis. The amplitude of the buckling mode shape was then included as a fraction of the steel tube thickness and,
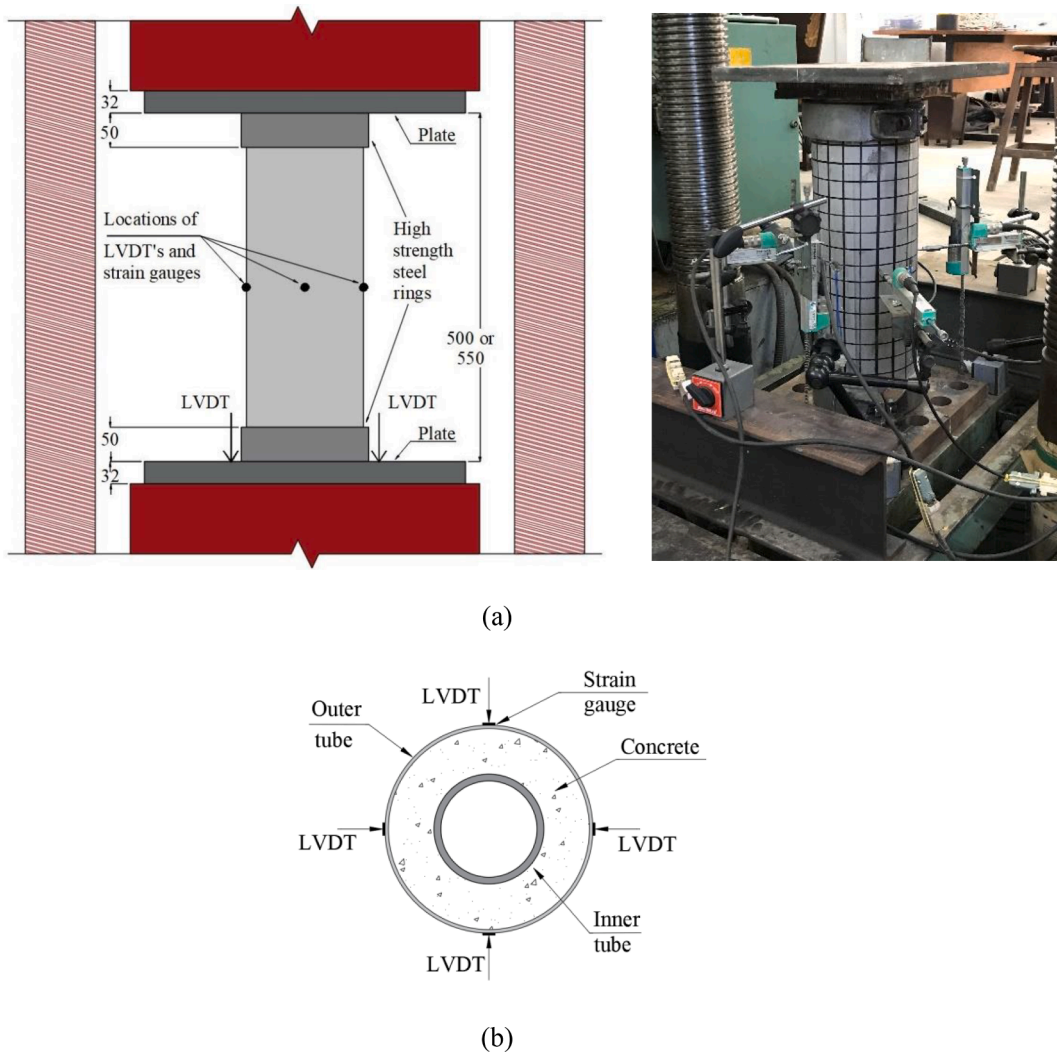
(a)

(b)

Fig. 7. Test arrangement showing (a) a schematic and photographic view in elevation (all dimensions are in mm) and (b) a cross-section view.

NAC1   NAC2   NAC3   NAC4   RAC1   RAC2   RAC3   RAC4

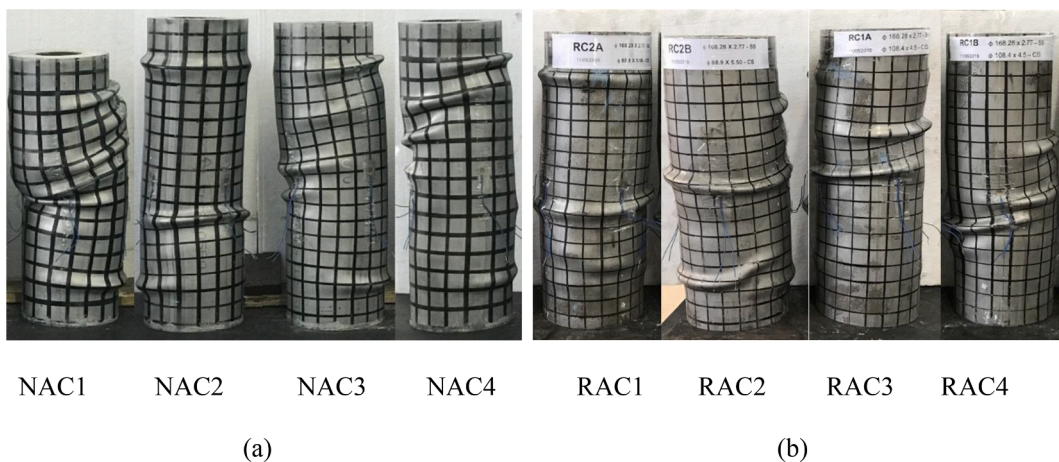(a)   (b)

Fig. 8. Specimens after testing showing outward-only local buckling of the outer stainless steel tube for stub columns with (a) NAC and (b) RAC infill.

following a sensitivity study, a value of $0.2t_{so}$ (≈ 0.5 mm) was employed. Both geometric and material nonlinearities were accounted for in the analyses which were solved using the modified Riks method [18]. The interface between the steel tubes and the concrete infill and also between the outer steel tube and the outer circular ring was simulated

using surface-to-surface contact in ABAQUS [18]. Hard contact was employed in the normal direction and a Coulomb friction model was used in the tangential direction, with a friction coefficient of 0.25, as recommended by Han *et al.* [12]. The average surface bond stress τ_b, given by Eq. (2), was also specified between the concrete and the steel

Fig. 9. Specimen RAC1 after testing showing inward-only local buckling of the carbon steel inner tube.

sections, based on the recommendations of Roeder *et al.* [32]:

$$\tau_b = 2.314 - 0.0195(D/t_{so}) \tag{2}$$

3.3. Material modelling

3.3.1. Concrete

The concrete infill was simulated using the concrete damage plasticity (CDP) model available in ABAQUS [18]. The compressive strength was taken from the concrete material tests conducted in the experimental programme. The Young's modulus E_c was determined in accordance with the method proposed by Gholampour *et al.* [33], as given by:

$$E_c = 0.016 \times (6.1 - 0.015R_c) \times (5.3 - 1.7w_{eff}/c)^{3.9} \tag{3}$$

in which R_c is the recycled aggregate replacement ratio, given as a percentage, and w_{eff}/c is the effective water-to-cement ratio. The stress–strain model for confined concrete in compression proposed by Tao *et al.* [34] was employed to simulate the infill material, as presented in Fig. 12 and described by Eqs. (4) and (5):

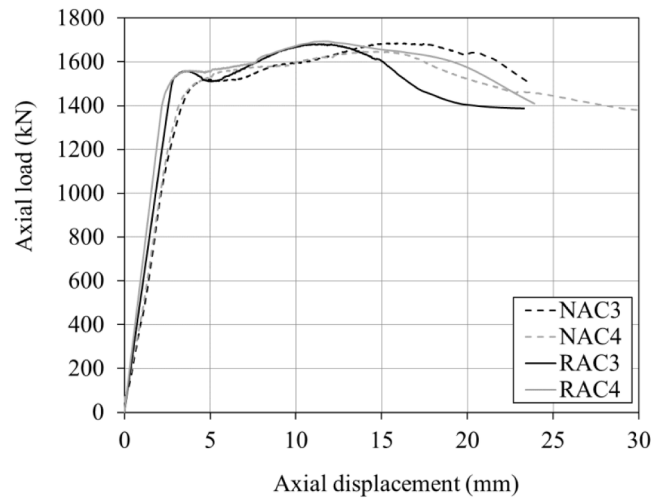$$\sigma = f_c \frac{AX + BX^2}{1 + X(A - 2) + X^2(B + 1)} \quad 0 < \varepsilon \le \varepsilon_{c0} \tag{4}$$

$$\sigma = f_r + (f_c - f_r)\exp\left[-\left(\frac{\varepsilon - \varepsilon_{cc}}{\alpha}\right)^\beta\right] \quad \varepsilon \ge \varepsilon_{cc} \tag{5}$$

where σ is the stress, f_c is the cylinder compressive strength of the concrete, $A = \frac{E_c\varepsilon_{c0}}{f_c}$, $B = \frac{(A-1)^2}{0.55} - 1$, X is the normalised strain calculated as $X = \frac{\varepsilon}{\varepsilon_{c0}}$, f_r is the stress at the end of the softening branch, α and β are
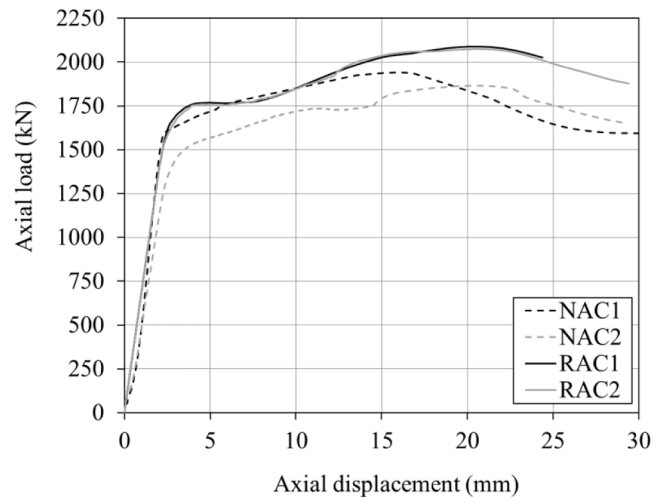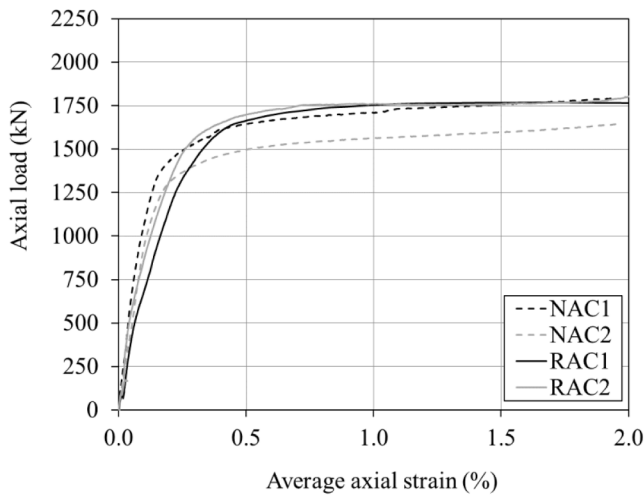

(a)

(b)

Fig. 10. Axial load *versus* axial displacement curves for the CFDST stub columns with (a) the smaller inner tubes and (b) the larger inner tubes.

parameters to determine the shape of the softening branch of the curve, ε_{c0} is determined from:
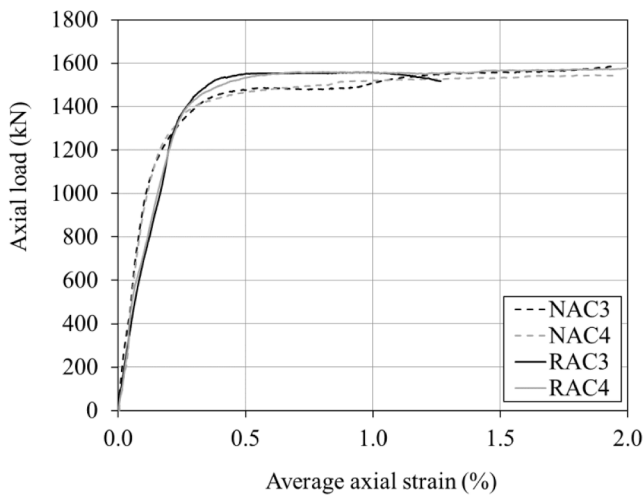
$$\varepsilon_{c0} = 0.00076 + \sqrt{(0.626f_c - 4.33) \times 10^{-7}} \text{ with } f_c \text{ in N/mm}^2 \tag{6}$$

and ε_{cc} is determined from:

$$\frac{\varepsilon_{cc}}{\varepsilon_{c0}} = e^k, \text{ with } k = (2.9224 - 0.00367f_c)\left(\frac{f_B}{f_c}\right)^{0.3124 + 0.002f_c} \text{ and } f_c \text{ and } f_B \text{ are in N/mm}^2 \tag{7}$$

where f_B is the confining stress provided to the concrete at Point B, calculated for circular CFST from:

(a)

(b)

Fig. 11. Axial load *versus* average axial strain for the CFDST stub columns with (a) the smaller inner tubes and (b) the larger inner tubes.

$$f_B = \frac{(1 + 0.027 f_y) e^{-0.02 \frac{D}{t}}}{1 + 1.6 e^{-10} f_c^{4.8}} \tag{8}$$

The parameters α, β and f_r were defined in accordance with the recommendations of Tao *et al.* [34]. Hence, α was determined from:

$$\alpha = 0.04 - \frac{0.036}{1 + e^{6.08 \xi_c - 3.49}}, \tag{9}$$

β was taken as 1.2 and f_r was obtained from.

$$f_r = 0.7 (1 - e^{-1.38 \xi_c}) f_c \leq 0.25 f_c \tag{10}$$

Note that although the constitutive model described by Eqs. (4)–(8) for confined concrete was initially developed for NAC, it was employed herein for RAC; this was considered to be appropriate since, as also observed in previous research [e.g., 35], no discernable difference in softening behaviour was evident from the tests performed on the confined NAC and RAC.

In addition to the stress–strain response, some additional parameters are required for the CDP model, including the dilatation angle ψ, eccentricity e_f, the ratio of the compressive strengths under biaxial and uniaxial loading f_{b0}/f_c and the stress invariant on the tensile meridian to
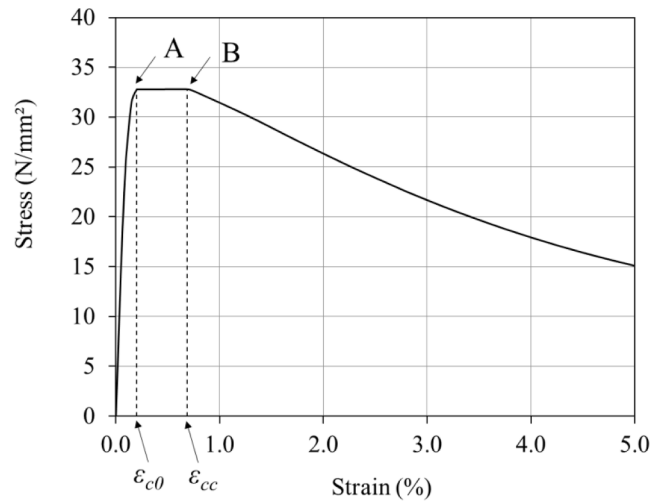

Fig. 12. Compressive stress–strain relationship for confined concrete adopted in FE model [34].

the compressive meridian K_c. These are assigned values of 36°, 0.1 and 1.16 for ψ, e_f and f_{b0}/f_c, respectively, based on the recommendations in the ABAQUS user's manual [18] and 2/3 for K_c, in accordance with Li *et al.* [36].

For the tensile properties of the concrete, the approach recommended by the Comite Euro-International du Beton (CEB-FIP Model Code) [37] was adopted, whereby the energy fraction G_f was determined for the confined concrete behaviour as:

$$G_f = \left(0.0469 d_{max}^2 - 0.5 d_{max} + 26\right) \left(\frac{f_c}{10}\right)^{0.7} \text{in N/m} \tag{11}$$

in which f_c is in N/mm² and d_{max} is the maximum coarse aggregate size in mm. It has been shown previously [36] that employing a fracture energy-based approach to simulate concrete tension stiffening behaviour is numerically more stable than alternative methods such as defining a post-failure stress–strain response.

3.3.2. Metal tubes

The measured material properties from the tensile coupon tests on the steel and stainless steel tubes described in Section 2 were incorporated into the FE simulations for the model validation. For the carbon steel inner tubes, only the key mechanical properties were provided by the manufacturer; the full stress–strain curve was therefore generated by using these values together with the constitutive model of Yun and Gardner [38]. For the stainless steel outer tubes, the full measured stress–strain curve was used. For both metal tubes, the engineering stress–strain curves were converted into true stress–true plastic strain curves using the expressions given in Eqs. (12) and (13) and inputted into ABAQUS [18]:

$$\sigma_{true} = \sigma_{nom}(1 + \varepsilon_{nom}) \tag{12}$$

$$\varepsilon_{ln}^{pl} = \ln(1 + \varepsilon_{nom}) - \frac{\sigma_{nom}}{E} \tag{13}$$

in which σ_{true} is the true stress, σ_{nom} is the engineering stress, ε_{ln}^{pl} is the logarithmic plastic strain and ε_{nom} is the engineering strain.
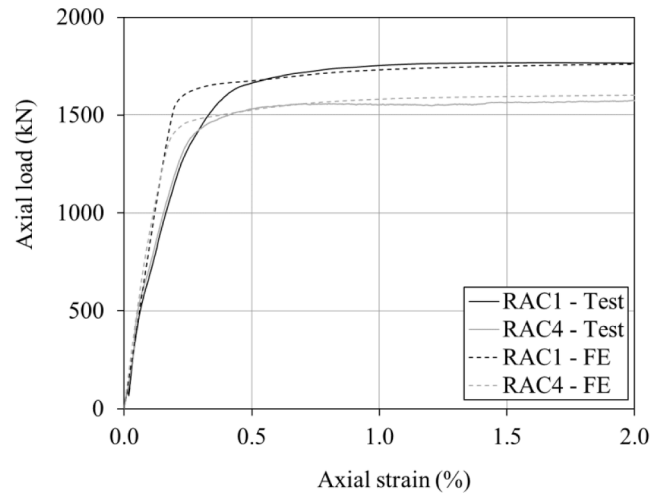
3.4. Validation of numerical model

The accuracy of the FE model was evaluated by comparing the full numerical load-deformation responses, ultimate loads and failure modes with those obtained from the physical tests reported herein as well as further experiments from the literature. Fig. 13 presents the axial load
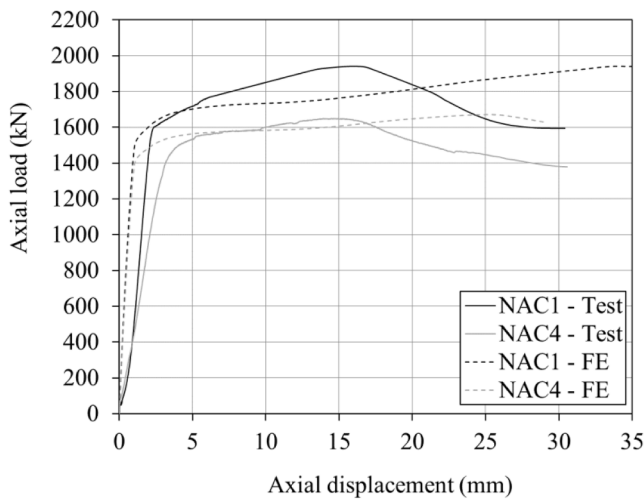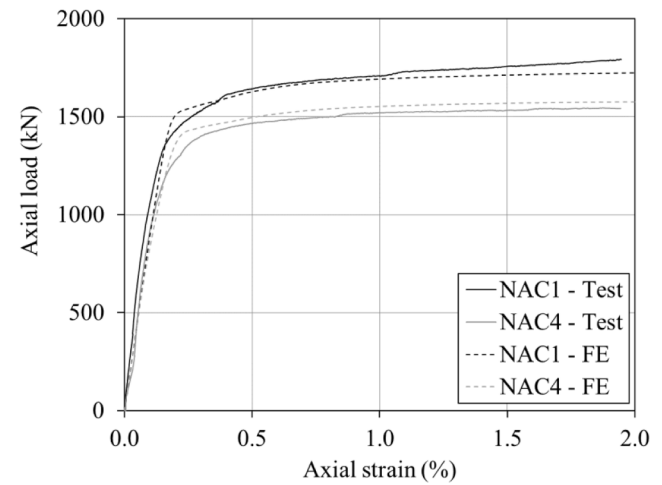
(a)

(a)
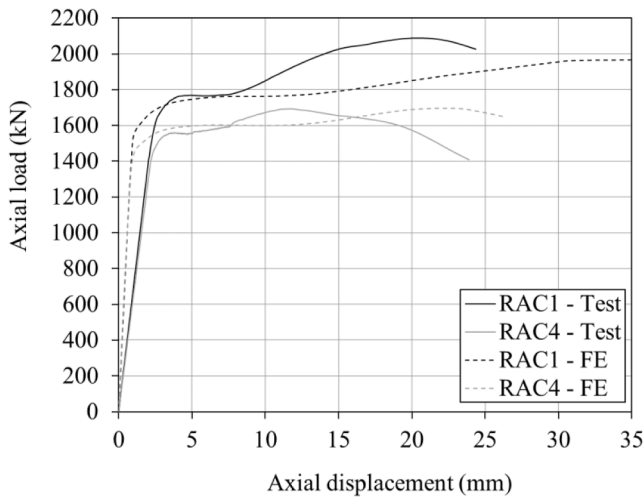
(b)

Fig. 13. Axial load *versus* axial displacement for the CFDST stub columns with (a) RAC and (b) NAC.

(b)

Fig. 14. Axial load *versus* axial strain for the CFDST stub columns with (a) RAC and (b) NAC.

et al. [39].

It can be seen from the results presented in Figs. 13 and 14 that the FE model provides a good representation of both the load–displacement and the load-axial strain responses of the test specimens, and captures the key behavioural features. The marginally lower initial slopes of the experimental curves shown in Fig. 13, relative to the FE curves, are attributed to possible non-uniform load introduction arising from slight deviations from flatness at the member ends or small gaps due to concrete shrinkage. Deviations in the form of the test and numerical load–displacement curves are attributed to the uncertainty surrounding the precise shape of the stress–strain curve (particularly the length of the yield plateau) of the hot-rolled steel tubes. With reference to the data in Table 4, it can be seen that the FE model provides an accurate and reliable prediction of the ultimate capacity of the stub columns, with a mean $N_{u,FE}/N_{u,test}$ value of 0.99 and a coefficient of variation (CoV) of 0.074. These values include the data from the experimental programmes of Wang *et al.* [13] and Han *et al.* [12]. In terms of the failure modes, Fig. 15 presents a comparison of the deformed shapes of RAC1 and RAC2 from (a) the experiments and (b) the FE model. The FE model can be seen to capture the experimentally observed outward-only local buckling of the outer stainless steel tube in the elevation view and the inward-

versus average axial displacement responses obtained experimentally and numerically for (a) specimens RAC1 and RAC4, and (b) NAC1 and NAC4. These were selected for brevity and the results are generally reflective of the behaviour for all specimens. In addition, Fig. 14 shows the corresponding axial load *versus* axial strain responses obtained experimentally and numerically. The ultimate loads from the tests $N_{u,test}$ and the corresponding values from the FE model $N_{u,FE}$ are presented in Table 4, together with the $N_{u,FE}/N_{u,test}$ ratios.

For further validation, eight tests from Wang *et al.* [13] and four tests from Han *et al.* [12] were also simulated using the FE model, and the results are given in Table 4. The tests from Wang *et al.* [13] were on CFDST stub columns with stainless steel outer tubes, high strength carbon steel inner tubes and conventional concrete for the infill. The tests from Han *et al.* [12] had stainless steel outer tubes, carbon steel inner tubes and conventional concrete for the infill. Note that the ultimate loads from the FE model were, in the absence of a peak, determined as the load at which the slope of the load *versus* axial displacement response reached 1% of its initial stiffness, as proposed by dos Santos

Table 4
Comparison of the ultimate loads from experiments and FE models.

| CFDST specimen	$N_{u,test}$ (kN)	$N_{u,FE}$ (kN)	$N_{u,FE}/N_{u,test}$
NAC1	1941	1940	1.00
NAC2	1865		1.04
NAC3	1649	1670	1.01
NAC4	1612		1.04
RAC1	2087	1966	0.94
RAC2	2075		0.95
RAC3	1685	1695	1.01
RAC4	1693		1.00
AC140 × 3-HC22 × 4 [13]	1410	1548	1.10
AC140 × 3-HC32 × 6 [13]	1423	1662	1.17
AC140 × 3-HC38 × 8 [13]	1626	1698	1.04
AC140 × 3-HC55 × 11 [13]	2543	2539	1.00
AC140 × 3-HC89 × 4 [13]	2025	1975	0.98
AC165 × 3-HC22 × 4 [13]	1750	1747	1.00
AC165 × 3-HC32 × 6 [13]	1943	1865	0.96
AC165 × 3-HC89 × 4 [13]	2375	2279	0.96
C1-1_220 × 3.62–159 × 3.72 [12]	2537	2439	0.96
C1-2_220 × 3.62–159 × 3.72 [12]	2566		0.95
C2-1_220 × 3.62–106 × 3.72 [12]	3436	2942	0.86
C2-2_220 × 3.62–106 × 3.72 [12]	3506		0.84
Mean			0.990
CoV			0.074

only local buckling of the inner carbon steel tube in the plan view. Overall, it is concluded that the FE model is capable of realistically representing the overall and ultimate behaviour of CFDST stub columns and thus is suitable for further parametric and design studies.

3.5. Parametric study

The validated numerical model is employed in the current section to develop a greater understanding of the influence of the key parameters on the behaviour of CFDST cross-sections in compression. The range of variables examined is given in Table 5. Throughout the parametric study, it was assumed that the stub columns were 500 mm in length, with austenitic stainless steel outer tubes and carbon steel inner tubes. The material properties of the steel tubes and the RAC were taken as those measured and reported in Section 2. A total of 36 analyses were

Table 5
Ranges of parameters investigated in the parametric study.

Parameter		Hollow ratio (χ)	Outer tube diameter D (mm)	Inner tube diameter d (mm)	Inner tube thickness t_{si} (mm)
Range	Maximum	0.87	219.1	168.3	5.5
	Minimum	0.28	141.3	60.3	4.5
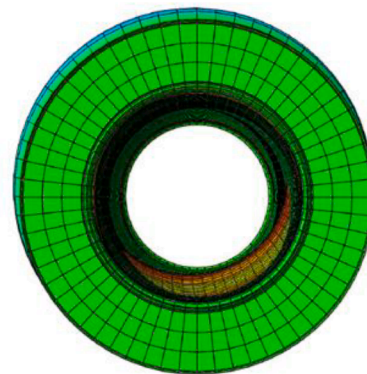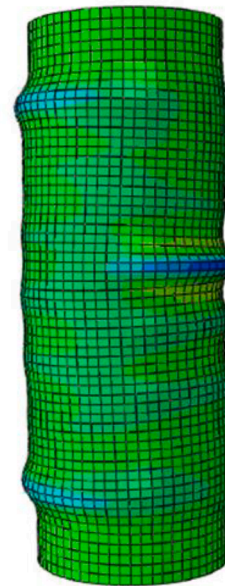
(a)

(b)

Fig. 15. Comparison of deformed shapes of RAC1 and RAC2 from (a) the experiments and (b) the FE model.

performed in the parametric study.

The ultimate compression resistance of CFDST cross-sections $N_{u,Han}$ can, as proposed by Han *et al.* [12], be considered as the sum of the capacities of the inner tube $N_{i,u}$ and the outer tube plus the sandwiched concrete combined $N_{osc,u}$, as given in Eq. (14):

$$N_{u,Han} = N_{i,u} + N_{osc,u} \tag{14}$$

The capacities of the two components in Eq. (14), $N_{i,u}$ and $N_{osc,u}$, are determined in accordance with Eqs. (15) and (16), respectively:

$$N_{i,u} = A_{si}f_{yi} \tag{15}$$

$$N_{osc,u} = A_{soc}f_{osc} \tag{16}$$

in which f_{yi} is the yield strength of the inner tube, A_{si} is the cross-sectional area of the inner tube, f_{osc} is a combined strength value for the outer stainless steel tube and the concrete infill, accounting for the confinement effect, and A_{soc} is the sum of the cross-sectional areas of the outer stainless steel tube A_{so} and the concrete A_c:

$$A_{soc} = A_{so} + A_c \tag{17}$$

The combined strength of the outer stainless steel tube and the infill concrete f_{osc} is given by Eq. (18):

$$f_{osc} = C_1\chi^2 f_{yo} + C_2(1.14 + 1.02\xi)f_c \tag{18}$$

in which χ is the hollow ratio determined using Eq. (1), f_{yo} is the yield (0.2% proof) strength of the outer stainless steel tube, with C_1 and C_2 given by Eqs. (19) and (20), respectively:

$$C_1 = \gamma/(1+\gamma) \tag{19}$$

$$C_2 = (1+\gamma_n)/(1+\gamma) \tag{20}$$

and ξ is the nominal confinement factor, determined from Eq. (21):

$$\xi = A_{sa}f_{yo}/A_{ce}f_c \tag{21}$$

In Eqs. (19) and (20), $\gamma = A_{so}/A_c$, where A_{so} is the cross-sectional area of the outer stainless steel tube and A_c is the cross-sectional area of the concrete, and $\gamma_n = A_{so}/A_{ce}$, where A_{ce} is an equivalent cross-sectional area of the sandwiched concrete, defined as the full area enclosed by the outer tube, given by:

$$A_{ce} = \pi(D - 2t_{so})^2/4 \tag{22}$$

The influence of the hollow ratio and the load-bearing contributions of the constituent components of CFDST cross-sections are assessed on the basis of the FE model results. The ultimate capacities $N_{u,FE}$ are typically examined in normalised form relative to the calculated resistance described above $N_{u,Han}$.

Two different hollow ratios χ were considered in the experimental programme, equal to either 0.55 or 0.67. In this section, the inner tube geometries are varied in the FE model to examine a wider range of χ between 0.28 and 0.87. With reference to the definition of the hollow ratio given in Eq. (1), it is noteworthy that a relatively small value of χ, i. e. close to zero, corresponds to an almost fully solid column and the behaviour is expected to be similar to that of a concrete filled steel tube (CFST). Meanwhile, when χ is relatively large, i.e. close to unity, the section behaves almost as a hollow steel-only section.

Fig. 16 presents the axial load $N_{u,FE}$ *versus* axial displacement responses for stub columns with a range of different hollow ratios; all of the stub columns have an outer tube diameter D and thickness t_{so} of 168.3 and 2.8 mm, respectively. The diameter of the inner tube d is varied to give a range of χ values, and the thickness t_{si} remains constant at 5.5 mm. It can be seen that, owing to the high level of restraint afforded to the outer stainless steel tube and the low slenderness of the inner steel tube, the CFDST cross-sections with the lower χ values exhibit a monotonically increasing load-deformation response and the highest resistance and ductility of the examined specimens. Conversely, the CFDST cross-sections with the higher χ values exhibit a distinct peak load owing to local buckling of the more vulnerable inner and outer tubes and the subsequent loss of confinement to the concrete.

Fig. 17 shows the normalized peak axial load ($N_{u,FE}/N_{u,Han}$) *versus* hollow ratio χ for a range of stub columns with different inner and outer diameters; the inner tube thickness is kept constant at 5.5 mm. The two dashed vertical lines represent the χ values of the test specimens, i.e. 0.55 and 0.67. For the recommended range of χ proposed by Han *et al.* [12], i.e. $0.5 < \chi < 0.7$, this design method is shown to provide a safe and accurate prediction of the capacity of CFDST sections with a stainless steel outer tube, carbon steel inner tube and RAC infill. Outside this range, the resistance predictions are somewhat conservative for low hollow ratios and marginally on the unsafe side for high hollow ratios.

In order to assess the relative contribution to the load-carrying capacity of each of the constituent elements in CFDST stub columns, Fig. 18 presents the axial load *versus* axial displacement responses for members with three different hollow ratios, namely (a) $\chi = 0.37$ (inner tube diameter of 60.3 mm), (b) $\chi = 0.55$ (inner tube diameter of 88.9 mm) and (c) $\chi = 0.87$ (inner tube diameter of 141.3 mm). All of the CFDST stub columns in these analyses have an outer tube with a diameter and thickness of 168.3 mm and 2.8 mm, respectively, and an inner tube which has a thickness of 4.5 mm.

The first clear observation is that the outer stainless steel tubes make a very similar contribution to the overall capacity for all of the χ values
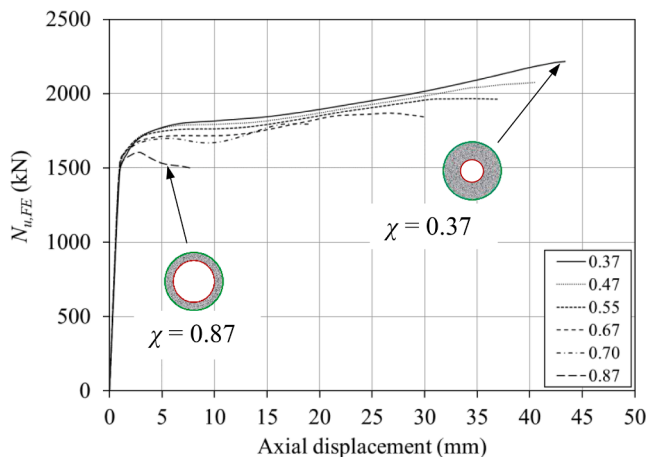

Fig. 16. Influence of hollow ratio χ on the axial load *versus* axial displacement response for CFDST columns with an outer diameter of 168.3 mm.
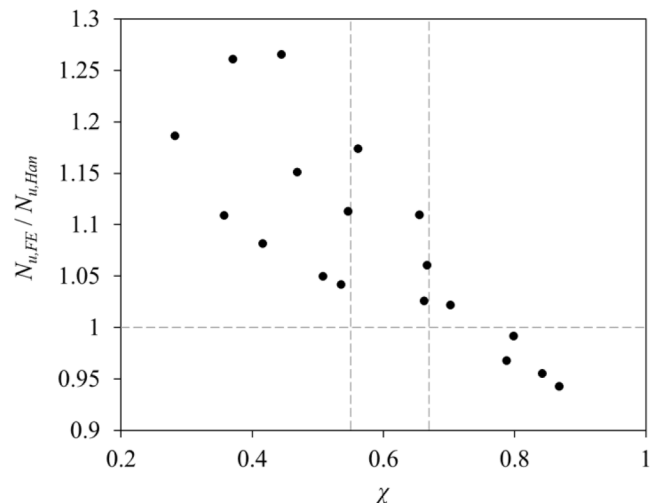

Fig. 17. Normalized FE axial capacities, relative to the Han *et al.* [12] resistance predictions, *versus* hollow ratio.
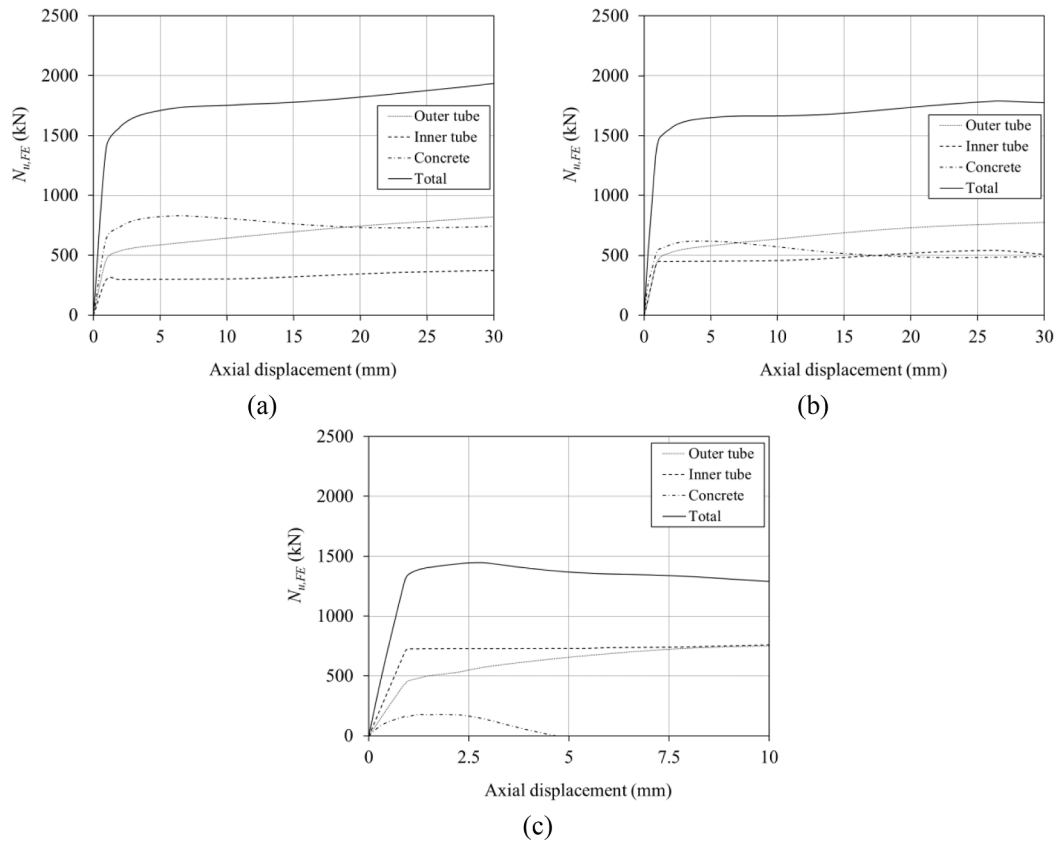
Fig. 18. Relative contribution to the axial load *versus* axial displacement response of each of the constituent structural components in CFDST stub columns with a hollow ratio of (a) $\chi = 0.37$, (b) $\chi = 0.55$ and (c) $\chi = 0.87$.

examined; this is as expected since this component remains constant for all of the analyses. Accordingly, the proportionate contribution made by the outer stainless steel tube to the overall stub column capacity compared to the other constituent elements varies slightly, but only as the overall axial load capacity changes in response to variation in the dimensions of the inner tube. On the other hand, the relative contributions of the inner carbon steel tube and the concrete infill to the overall capacity for different hollow ratios vary quite considerably. For CFDST stub columns with a hollow ratio of 0.87, the inner tube diameter is quite large and the volume of infill concrete is comparatively low. Therefore, the inner tube makes a relatively large contribution to the overall capacity, while the concrete makes a very small contribution; the reverse is true for the low hollow ratio of 0.37.

4. Design of CFDST stub columns

The design of concrete-filled double skin tubular columns is not yet included in international design standards. Nevertheless, reflecting the increasing interest in the use of these members in recent years, different design methods have been proposed in the literature, two of which are assessed herein. The first method was proposed by Han *et al.* [12] and has already been discussed in this paper. The predicted load capacity $N_{u,Han}$ is given in Eq. (14). The second method was developed by Wang *et al.* [13] and is an adaptation of the existing Eurocode 4 Part 1–1 [40] design rules, as given in Eq. (23):

$$N_{u,Wang} = A_{sa}f_{0.2} + 0.85A_cf_c + A_{si}f_y \tag{23}$$

where $N_{u,Wang}$ is the predicted load-bearing capacity and A_{so}, A_{si} and A_c are the cross-sectional areas of the stainless steel outer tube, carbon steel inner tube and concrete, respectively.

The experimental ($N_{u,Exp}$) and FE ($N_{u,FE}$) capacities discussed
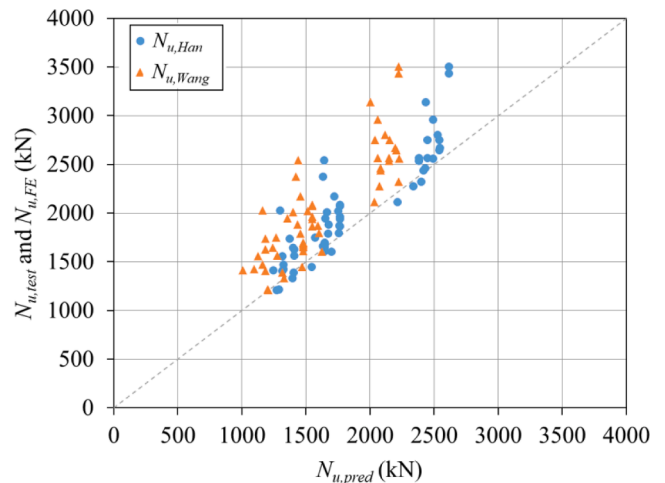

Fig. 19. Evaluation of accuracy of existing design expressions for CFSDT sections.

previously in this paper are compared with the corresponding predicted $N_{u,pred}$ values ($N_{u,Han}$ and $N_{u,Wang}$) in Fig. 19. Both design expressions can be seen to provide good predictions of the experimental and numerical results. The Wang *et al.* [13] predictions are slightly more scattered, with a coefficient of variation (CoV) of 0.147, compared to the Han *et al.* [12] predictions, with a CoV of $N_{u,test}/N_{u,Han}$ of 0.125. The Han *et al.* [12] expression leads to more predictions on the unsafe side though these generally correspond to geometries that lie outside of the recommended range of χ values set out by Han *et al.* [12], i.e. $0.5 < \chi < 0.7$.

5. Conclusions

A detailed analysis of the behaviour and design of CFDST stub columns comprising a stainless steel outer tube, carbon steel inner tube, and concrete infill made using either normal aggregates or recycled aggregates has been presented. The study features both experimental and numerical investigations. A total of eight tests were conducted on CFDST stub columns, four of which contained normal concrete and four of which contained concrete made from recycled aggregates. In addition to the tests, an FE model was developed and validated using the test results from the current paper as well as others from the literature. The validated FE model was then used to perform parametric studies.

The key observations from the present investigation are summarised as follows:

- The results show for the first time that CFDST stub columns made with recycled aggregate concrete behave in a similar manner to those with normal concrete. It is recommended that RAC is employed more commonly in CFDST stub columns, in order to achieve more sustainable construction.
- CFDST cross-sections with relatively low χ values exhibit a monotonically increasing load-deformation response, as well as higher resistance and ductility, compared with cross-sections with higher hollow ratios, but generally require greater material usage. This is attributed to the high level of restraint afforded to the outer stainless steel tube and the low slenderness of the inner steel tube. On the other hand, the CFDST cross-sections with higher χ values exhibit a distinct peak load owing to local buckling of the more vulnerable inner and outer tubes and the subsequent loss of confinement to the concrete.
- Although the design of CFDST stub columns is not explicitly covered by current design methods, researchers have proposed design methods owing to the increasing interest in these section types [12,13]. The design method of Wang *et al.* [13] provides resistance predictions which are in good agreement with the FE and experimental results over the full range of considered hollow ratios χ. The predictions [13] are slightly more scattered that those obtained from Han *et al.* [12], but fewer are on the unsafe side.
- The design method proposed by Han *et al.* [12] within the recommended range of χ, i.e. $0.5 < \chi < 0.7$, provides a safe and accurate prediction of the capacity for CFDST sections with a stainless steel outer tube, carbon steel inner tube and RAC infill. Outside this range, the resistance predictions are somewhat conservative for low hollow ratios and marginally on the unsafe side for high hollow ratios.

Declaration of Competing Interest

The authors declare that they have no known competing financial interests or personal relationships that could have appeared to influence the work reported in this paper.

Acknowledgements

References

[1] Wei S, Mau ST, Vipulanandan C, Mantrala SK. Performance of new sandwich tube under axial loading: experiment. J Struct Eng 1995;121(12):1806–14.

[2] Li W, Han L-H, Zhao X-L. Axial strength of concrete-filled double skin steel tubular (CFDST) columns with preload on steel tubes. Thin-Walled Struct 2012;56:9–20.

[3] Tao Z, Han L-H, Zhao X-L. Behaviour of concrete-filled double skin (CHS inner and CHS outer) steel tubular stub columns and beam-columns. J Constr Steel Res 2004; 60(8):1129–58.

[4] Lu H, Han L-H, Zhao X-L. Fire performance of self-consolidation concrete filled double skin steel tubular columns: experiments. Fire Saf J 2010;45:106–15.

[5] Ayough P, Ramli Sulong NH, Ibrahim Z. Analysis and review of concrete-filled double skin steel tubes under compression. Thin-Walled Struct 2020;148:106495.

[6] Gardner L. Stability and design of stainless steel structures – review and outlook. Thin-Walled Struct 2019;141:208–16.

[7] Wang F-C, Han L-H, Li W. Analytical behavior of CFDST stub columns with external stainless steel tubes under axial compression. Thin-Walled Struct 2018;127: 756–68.

[8] McGinnis MJ, Davis M, de la Rosa A, Weldon BD, Kurama YC. Strength and stiffness of concrete with recycled concrete aggregates. Constr Build Mater 2017;154: 258–69.

[9] Silva RV, de Brito J, Dhir RK. Properties and composition of recycled aggregates from construction and demolition waste suitable for concrete production. Constr Build Mater 2014;65:201–17.

[10] Silva RV, de Brito J, Dhir RK. Establishing a relationship between modulus of elasticity and compressive strength of recycled aggregate concrete. J Cleaner Prod 2016;112:2171–86.

[11] Wardeh G, Ghorbel E, Gomart H. Mix design and properties of recycled aggregate concretes: applicability of eurocode 2. Int J Concr Struct Mater 2014;9:1–20.

[12] Han L-H, Ren Q-X, Li W. Tests on stub stainless steel-concrete-carbon steel double-skin tubular (DST) columns. J Constr Steel Res 2011;67(3):437–52.

[13] Wang F, Young B, Gardner L. Compressive testing and numerical modelling of concrete-filled double skin CHS with austenitic stainless steel outer tubes. Thin-Walled Struct 2019;141:345–59.

[14] Hassanein MF, Kharoob OF, Liang QQ. Circular concrete-filled double skin tubular short columns with external stainless steel tubes under axial compression. Thin-Walled Struct 2013;73:252–63.

[15] Uenaka K, Kitoh H, Sonoda K. Concrete filled double skin circular stub columns under compression. Thin-Walled Struct 2010;48(1):19–24.

[16] Chen Z, Xu J, Xue J, Su Y. Performance and calculations of recycled aggregate concrete-filled steel tubular (RACFST) short columns under axial compression. Int J Steel Struct 2014;14(1):31–42.

[17] P.F. Rodrigues. Avaliação experimental e numérica de colunas tubulares mistas CFDST (aço inoxidável-concreto-aço carbono), MSc Dissertation, PGECIV – Post Graduate Program in Civil Engineering, State University of Rio de Janeiro – UERJ, 2018 (in Portuguese).

[18] ABAQUS, ABAQUS/standard User's Manual. Version 6.17, Dassault Systemes Simulia Corp., USA, 2017.

[19] Joseph M, Boehme L, Sierens Z, Vandewalle L. Water absorption variability of recycled concrete aggregates. Mag Concr Res 2015;67(11):592–7.

[20] Silva RV, de Brito J, Dhir RK. The influence of the use of recycled aggregates on the compressive strength of concrete: a review. Eur J Environ Civ Eng 2015;19(7): 825–49.

[21] B.N.T. De Macedo. Determinação do coeficiente de conformação superficial de barras de aço para uso em concreto armado, MSc Dissertation, PGECIV – Post Graduate Program in Civil Engineering, State University of Rio de Janeiro – UERJ, 2018 (in Portuguese).

[22] ABNT NBR 7251. Agregados em estado solto – Determinação da massa unitária – Método de ensaio, Associação Brasileira de Normas Técnicas, Rio de Janeiro, Brazil (in Portuguese), 1982.

[23] ABNT NBR NM 45. Agregados – Determinação da massa unitária e do volume de vazios, Associação Brasileira de Normas Técnicas, Rio de Janeiro, Brazil (in Portuguese), 2006.

[24] ABNT NBR NM 52. Agregado miúdo – Determinação de massa específica e massa específica aparente, Associação Brasileira de Normas Técnicas, Rio de Janeiro, Brazil (in Portuguese), 2002.

[25] EN 10002-1:1990. Metallic materials – Tensile testing – Part 1: Method of test at ambient temperature. CEN, European Committee for Standardization, Brussels.

[26] Huang Y, Young B. The art of coupon tests. J Constr Steel Res 2014;96:159–75.

[27] Luquin IA. New approach for efficient design of stainless steel RHS and SHS elements. Barcelona, Spain: Universitat Politècnica de Catalunya; 2016. Ph.D. thesis.

[28] X. Meng and L. Gardner. Cross-sectional behaviour of cold-formed high strength steel circular hollow sections. Thin-Walled Structures. 156 (2020) 106822.

[29] E. Mirambell, E. and E. Real. On the calculation of deflections in structural stainless steel beams: an experimental and numerical investigation. Journal of Constructional Steel Research (2000) 54(1):109-133.

[30] Rasmussen KJR. Full-range stress–strain curves for stainless steel alloys. J Constr Steel Res 2003;59(1):47–61.

[31] Wang F, Young B, Gardner L. Compressive behaviour and design of CFDST cross-sections with stainless steel outer tubes. J Constr Steel Res 2020;170:105942.

[32] Roeder CW, Cameron B, Brown CB. Composite action in concrete filled tubes. J Struct Eng 1999;125:77–484.

[33] Gholampour A, Gandomi AH, Ozbakkaloglu T. New formulations for mechanical properties of recycled aggregate concrete using gene expression programming. Constr Build Mater 2017;130:122–45.

[34] Tao Z, Wang Z-B, Yu Q. Finite element modelling of concrete-filled steel stub columns under axial compression. J Constr Steel Res 2013;89:121–31.

[35] Z.W. Guan, A.S. Al-Husainy, M. Al Teneiji, .Y. Wang. Concentric and Eccentric Compression Behaviour of Recycled Aggregate Concrete Filled Steel Tube Columns Strengthened with CFRP. Applied Composite Materials (2022).

[36] W. Li, L-H. Han, T-M. Chan. Numerical investigation on the performance of concrete-filled double-skin steel tubular members under tension, Thin-Walled Structures. 79 (2014) 108-118.

[37] FIP. CEB-FIP Model Code 1990. London: Thomas Telford Ltd. (1993).

[38] Yun X, Gardner L. Stress-strain curves for hot-rolled steels. J Constr Steel Res 2017; 133:36–46.

[39] dos Santos GB, Gardner L, Kucukler M. A method for the numerical derivation of plastic collapse loads. Thin-Walled Structures 2018;124:258–77.

[40] EN 1994-1-1: 2004. Design of Composite Steel and Concrete Structures, Part 1.1: General Rules and Rules for Buildings. CEN, European Committee for Standardization, Brussels.